Frequency-Coded Passive Multifunctional Elastic Metasurfaces

Junjie Rong, Wenjing Ye,* Shengyuan Zhang, and Yijun Liu

As an emerging material, metasurfaces open the door to a wide range of applications based on ultrasonic and elastic waves. However, most of the existing elastic metasurfaces have a fixed functionality and operate at a fixed frequency, which make them difficult to adapt to changing working requirements and/or environments. Although several recently proposed reconfigurable designs can relax this limitation, they either need laborious tuning or complex active control systems. In this work, by encoding multiple functionalities onto a single metasurface through operation frequencies, passive metasurfaces with switchable multifunctionalities are proposed and realized. Different wave manipulation functions of a single metasurface can be switched from one to another simply by changing the operation frequency. The design of these metasurfaces is realized using a systematic design approach based on topology optimization. Frequency-coded multiple elastic wave manipulation functions, including wave beam steering and focusing, are numerically and experimentally demonstrated. Good agreement between the numerical simulations and experimental measurements is achieved. The proposed design strategy significantly enhances the functionalities and adaptivity of metasurfaces, moving them closer towards real-world applications.

1. Introduction

In the past decade, metamaterials have experienced a rapid development due to their unique properties that cannot be found in natural materials. These properties have greatly enhanced wave manipulation capabilities. In particular, metasurfaces, as a type of planar gradient metamaterials, have attracted a great deal of attentions due to their compact form. Governed by generalized Snell's law,[1] these materials modulate the wavefront by relying on gradually accumulated phase changes along the metasurface. The development of metasurfaces was initiated in the electromagnetic field and then extended to acoustic and elastic wave fields. A variety of novel wave manipulation functionalities have since been realized, for example, wave beam steering and focusing,[2–4] perfect absorption or insulation,[5,6] acoustic/optical holograms[7] and carpet cloaking.[8] For elastic wave, metasurfaces offer new possibilities to a wide range of applications spanning from nondestructive evaluation, energy harvesting,[9] to acoustic tweezers for microparticle manipulation.[10]

One of the challenges in applying metamaterials to real-word applications is their lack of adaptivity to different functional needs. Most existing metasurfaces were designed at a fixed frequency and have only a single fixed function. To address this issue, reconfigurable and programmable metamaterials have been developed recently. These metamaterials generally resort to active or mechanically alterable elements that are mutable to certain external stimuli to realize the adaptivity.[11–14] Some of them harness mechanical instability to change unit-cell's configuration and thus the functionality can be switched from one to another using external loadings, which can be either mechanical or thermal loading.[11,15–17] Other reconfigurable or programmable approaches include tunable nonlinear deformation,[12,13] origami-inspired metamaterials,[18] piezo shunting,[14] and others. With respect to metasurfaces, Memoli et al. proposed the concept of quantized metasurface, in which the premanufactured metamaterial bricks could be reassembled to realize different acoustic wave steering.[19] Very recently, a continuously programmable acoustic metasurface was reported.[20] The phase shift produced by each unit cell of this metasurface is independently tuned using a fluidic system. There are a few other designs of acoustic[21,22] and elastic[23] metasurfaces using the similar concept but with different mechanical mechanisms, for example, by manually adjusting the structure to change the acoustic channel length or the resonance frequency. Piezoelectric materials were also used to achieve tunability.[24,25] Real-time tunability was demonstrated using a sophisticated feed-back control system.[25]

All of the aforementioned approaches either alter the geometry of the structure manually or need an external element/system to control the condition of the system, which may be difficult or too costly to realize in some practical applications.

Dr. J. Rong, Prof. W. Ye, S. Zhang
Department of Mechanical and Aerospace Engineering
The Hong Kong University of Science and Technology
Clear Water Bay, Kowloon, Hong Kong, China
E-mail: mewye@ust.hk

Dr. J. Rong
School of Astronautics
Northwestern Polytechnical University
Xi'an, Shaanxi 710072, China

Prof. Y. Liu
Department of Mechanics and Aerospace Engineering
Southern University of Science and Technology
Shenzhen 518055, China

The ORCID identification number(s) for the author(s) of this article can be found under https://doi.org/10.1002/adfm.202005285.

**ADVANCED
SCIENCE NEWS**
www.advancedsciencenews.com

**ADVANCED
FUNCTIONAL
MATERIALS**
www.afm-journal.de

Moreover, these approaches are difficult to be scaled down to suit to microscale applications such as on-chip elastic/acoustic wave devices.[26] An alternative approach to realize multifunctionality, which is often termed as multiplexing technique in the optical community,[27,28] is to design structures whose responses are tailored for different states of the incident wave such as amplitudes, frequencies, polarizations, etc. Switching between different functionalities is then achieved by changing the state of the incident wave. For example, a tunable acoustic topological insulator was proposed[29] in which the tunability is derived from an energy-dependent band structure. Hence the insulator can be activated simply by the input energy, that is, wave amplitude. Multiplexed metasurface experienced a rapid development in the optical community in recent years. Several types of multiplexing metasurfaces have been developed, resulting in various novel materials such as polarization-controlled,[30,31] frequency-selective,[32,33] angle-selective,[34] and helicity-multiplexed[35] metasurfaces.

In this work, for the first time, we design and realize frequency-multiplexed elastic metasurfaces that possess of multiple wave-manipulation functionalities. To this end, multiple target wave functionalities are encoded onto different frequencies. The switch between functionalities can be achieved simply by changing the input frequency. The design is purely passive and no geometrical reconfiguration and control systems are needed. Using frequency to control functionalities been demonstrated on acoustic metasurfaces designed for controlling reflected waves.[36–38] These metasurfaces consist of multiple Helmholtz resonant units, which are well-decoupled and merely work in the vicinity of their respective resonant frequencies. Therefore, independent control of phases at different frequencies can be realized. However, the extension of this mechanism to manipulating elastic waves in solid is not straightforward. In addition, other design requirements that are crucial in practical applications such as high transmission efficiency,[3,39] robust performance should be considered, which further complicates the design.

Here, in contrast to previous designs, we make use of the concept of free-form material design based on an inverse design methodology entitled topology optimization (TO). The TO, which was originated from and subsequently matured in the structural optimization community,[40] recently been applied to the design and discovery of novel metamaterials.[41–44] By allowing the geometry to be freely optimized, TO maximizes the design space and allows efficient exploration of beneficial structures that meets multiple objectives and requirements. With this powerful technique, we have successfully designed and experimentally demonstrated metasurfaces with multiple functionalities encoded on two and three frequencies. The proposed frequency-coded metasurface mechanism and design approach will open new possibilities for a wide range of elastic wave applications such as acoustic tweezers and holograms.

2. Results

2.1. Inverse Design Approach

Metasurface works by realizing a specific phase profile along its surface when the wave propagates through it. In this work,

a designed single metasurface can realize different phase profiles independently at multiple target frequencies. In this way, multiple functions are encoded onto different frequencies, achieving frequency-selective wave manipulation.

Figure 1 shows a schematic diagram illustrating the design strategy. The metasurface to be designed is a thin single-phase material consisting of arrays of unit cells. Each row of the metasurface contains four identical unit cells, which are designed to modulate the phase of transmission waves. Unit cells in different rows are different and are arranged to produce specific phase profiles required for certain functionalities. We design each row individually, with the objective of achieving several specific phase shifts $\phi_{c1}^{\mathrm{tar}}, \phi_{c2}^{\mathrm{tar}} \cdots$ at different target frequencies, denoted as $\omega_{c1}, \omega_{c2} \cdots$. Hence the design domain for each row is one unit cell as shown in Figure 1a. Here, the key feature that distinguishes our design from most existing works is that the designed unit cell should be able to produce specific but different phase shifts at different target frequencies as shown in Figure 1c. Therefore, multiple functionalities can be realized independently at different target frequencies by producing different phase shift profiles. In contrast to most passive metasurfaces which can only operate at one frequency once fabricated, the proposed design scheme allows one metasurface to possess multifunctionalities switchable by the input frequency. To use identical unit cells in each row allows the optimizer explores the periodicity in the horizontal direction so as to enhance the wave transmission.[45] In addition, the design space is significantly reduced compared to the case in which each cell is different in the same row.

In this work, we consider metasurfaces for controlling in-plane elastic wave propagation in solid medium. Plane stress condition is assumed. The design of each unit cell is carried out using TO in which the design domain is discretized into a set of uniform elements. The density of each element is an independent design variable and is found by minimizing the objective function defined as a summation of the deviations to the target phase shifts at the target frequencies, that is

$$\min\left(g = g_{\omega_{c1}} + g_{\omega_{c2}} + \cdots = \frac{\left|\phi_{c1} - \phi_{c1}^{\mathrm{tar}}\right|}{\pi} + \frac{\left|\phi_{c2} - \phi_{c2}^{\mathrm{tar}}\right|}{\pi} + \cdots \right) \qquad (1)$$

where ϕ_{ci} and ϕ_{ci}^{tar}, $i = 1, 2, \cdots$ are the phase shift produced by the unit cell and the target phase shift at the frequency ω_{ci} respectively. In addition to producing desired phase shifts, high transmission and robust performance over operation frequencies are necessary for achieving good performance in practical applications.[45] Therefore, additional requirements have to be added to the objective function. To this end, instead of demanding the desired phase profiles to be achieved at only the target frequencies, the objective function is modified so that desired phase profiles can be achieved within a frequency interval with a bandwidth around 10% centered at each target frequency ω_{ci}. Taking one target frequency ω_c as an example, the objective function takes the form of

$$g_{\omega_c} = \sum_{j}^{N_\omega} \left(w_j^\phi \delta\phi_j + w_j^T \delta T_j \right) \qquad (2)$$
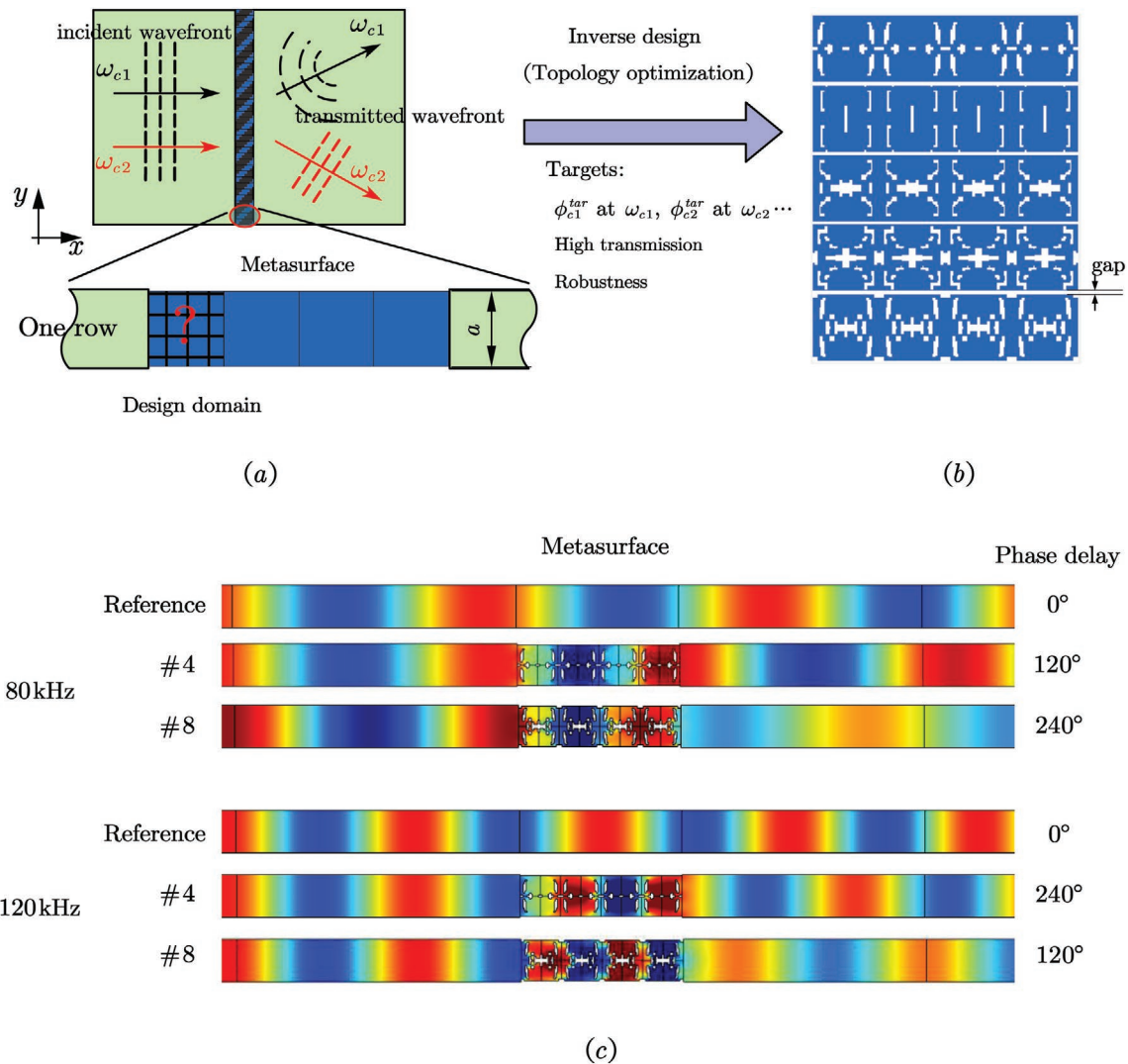
Figure 1. Schematic illustration of the design approach for frequency-coded metasurface. a) Schematic illustration of functions of a frequency-coded metasurface. The enlarged inset shows the sandwich model used to perform optimization for the design of one row of the metasurface. The meshed unit cell shows the initial design domain. b) A part of the designed metasurface described in Section 2.2.1. The blue color represents solid material and the white color represents void. c) Simulated wave field of x component of displacement field to demonstrate phase shifts produced by two unit cells (#4, #8 in Table 1) at the two target frequencies of 80 and 120 kHz.

where N_ω is the number of sampling frequencies within the frequency interval centered at ω_c. $\delta\phi_j$ and δT_j are deviations from the target phase shifts and target transmission, that is, 1, at the j-th sampling frequency, defined as $\delta\phi_j = |\phi_j - \phi_j^{tar}|/\pi$ and $\delta T_j = |T_j - 1|$. w_j^ϕ and w_j^T are the two weighting parameters.

The target phase shifts $\phi_j^{tar}, j = 1, \cdots N_\omega$ are determined by the desired phase gradient profile. As mentioned previously, robustness over operation frequency is one design requirement. This means that the same refraction angle should be achieved within the frequency interval considered. Hence the metasurface works not only under harmonic excitations but also for short tone burst signals. Based on the generalized Snell's law, the target phase shifts are set by a linear equation with respect to the frequency as

$$\phi_j^{tar} = \frac{\omega_j \left(f(\gamma) + \delta\phi \right)}{\omega_c} - \delta\phi \tag{3}$$

where $f(\gamma)$ is determined from the desired refraction angle profile along the metasurface and $\delta\phi$ is a user-defined parameter which is constant for all unit cells. This formula, Equation (3), complies with the condition for robustness proposed recently.[45]

To determine $\delta\phi$, let us examine the physical meaning of Equation (3). Given the wave number k of the corresponding propagation mode inside the metasurface, the phase delay produced by the metasurface can be approximately expressed as

$$\phi \approx (k - k_0) d \tag{4}$$

where $k_0 = \omega/c_0$ is the wave number of the host material and d is the thickness of the metasurface. By substituting Equation (4) into the target phase delay Equation (3), the dispersion relation of the metasurface can be obtained as

ADVANCED
SCIENCE NEWS
www.advancedsciencenews.com

ADVANCED
FUNCTIONAL
MATERIALS
www.afm-journal.de

Table 1. Designed unit cells and corresponding target phase shifts at two frequencies. The black color represents solid material and the white color represents void.

Unit cell index	0	1	2	3	4	5
$\phi_{\omega 1}^{tar}$	0°	30°	60°	90°	120°	150°
$\phi_{\omega 2}^{tar}$	360°	330°	300°	270°	240°	210°
Structure of unit cell						
Unit cell index	6	7	8	9	10	11
$\phi_{\omega 1}^{tar}$	180°	210°	240°	270°	300°	330°
$\phi_{\omega 2}^{tar}$	180°	150°	120°	90°	60°	30°
Structure of unit cell						

$$k = \left(\frac{f(\gamma) + \delta\phi}{d} + \frac{1}{c_0} \right)\omega - \frac{\delta\phi}{d} \qquad (5)$$

Equation (5) describes the linear dispersion that needs to be achieved within the frequency interval considered. The parameter $\delta\phi$ influences the intercept and the slope of the target dispersion curve. It should be chosen so that the linear dispersion is easier to achieve within the frequency interval. Based on our experience, for large target frequencies, a large value of $\delta\phi$ has such as 2π will make the objective more achievable.

It should be noted that the generalized Snell's law[1] only requirements on the gradient of the phase profile along the metasurface. Thus, the combination of unit cells to realize the same function is not unique. The TO problem is solved by a binary-coded genetic algorithm in this work. A detailed description on the developed TO algorithm is provided in Section 4.

2.2. Two-Frequency Results

In this section, we present two design cases related to the manipulation of longitudinal elastic waves in an aluminum medium. One is to demonstrate frequency-selective wave beam steering and the other is to demonstrate frequency-selective wave focusing. Metasurfaces are made of the same material as the host medium, with its Young's modulus being 69 GPa, density being 2700 kg · m^{-3} and Poisson's ratio being 0.3. Plane stress condition is assumed in the design. As shown in Figure 1, the metasurface consists of four layers of square-shaped unit cells in the x direction and a thickness of 3.8 cm. Unit cells in different rows are designed separately and may have very different structures. When they are assembled to form the metasurface, the interaction between two neighboring rows could distort the wavefront. In order to eliminate such interactions, a thin gap of 5×10^{-3}m was placed between two neighboring rows of unit cells as shown in Figure 1b. Results corresponding to two-frequency designs are presented in this section. Those corresponding to three-frequency design case are presented in Section S3 in the Supporting Information. The two target center frequencies are $\omega_{c1} = 80$ kHz and

$\omega_{c2} = 120$ kHz, respectively. Centered at these two target frequencies, a frequency range with a bandwidth of 10 kHz is chosen, which is discretized into $N_\omega = 5$ sample frequencies. The parameter $\delta\phi$ in Equation (3) is set as 0 for the low frequency group with $\omega_{c1} = 80$ kHz and as 2π for the high frequency group with $\omega_{c2} = 120$ kHz.

2.2.1. Frequency-Dependent Wave Beam Steering

In this example, a metasurface that is able to selectively refract elastic waves of two different frequencies into two different directions is demonstrated. Two linear phase profiles are realized at two frequency groups centered at 80 and at 120 kHz. The gradients of the two linear profiles are $\pm \pi/6a$, respectively, where a is the height of the unit cell as shown in Figure 1a. According to the generalized Snell's law, the refraction angles of normal incident waves corresponding to the two phase profiles should be 33.5° and $-21.6°$, respectively.

Twelve unit cells with their phase shifts covering the full range of [0, 2π] are designed and shown in **Table 1**. These 12 unit cells form one supercell in the metasurface, capable of providing the required phase gradients. **Figure 2** plots the transmission coefficients and phase shifts of these unit cells at a few selected frequencies calculated from the finite element method (FEM) simulations. It can be observed that the realized phase shifts agree well with the target values in general. Apart from a few cases with relatively low energy transmission, most cases have near unity transmission, resulting in average transmission coefficients of 0.86 and 0.95 at the two frequency groups respectively.

In the following, we show how the desired different phase delays are achieved at the two target frequencies from the perspective of wave dispersion band structure. **Figure 3** plots the band structures of unit cell #4 and #6 listed in Table 1. As a comparison, the target dispersion curves obtained by Equation (5) are also presented. It is observed that the dispersion curves of the two unit cells fit well with the target curves (Equation (5)) within the two frequency intervals. For unit cell #4, both the center frequencies lie in the same longitudinal mode; while for
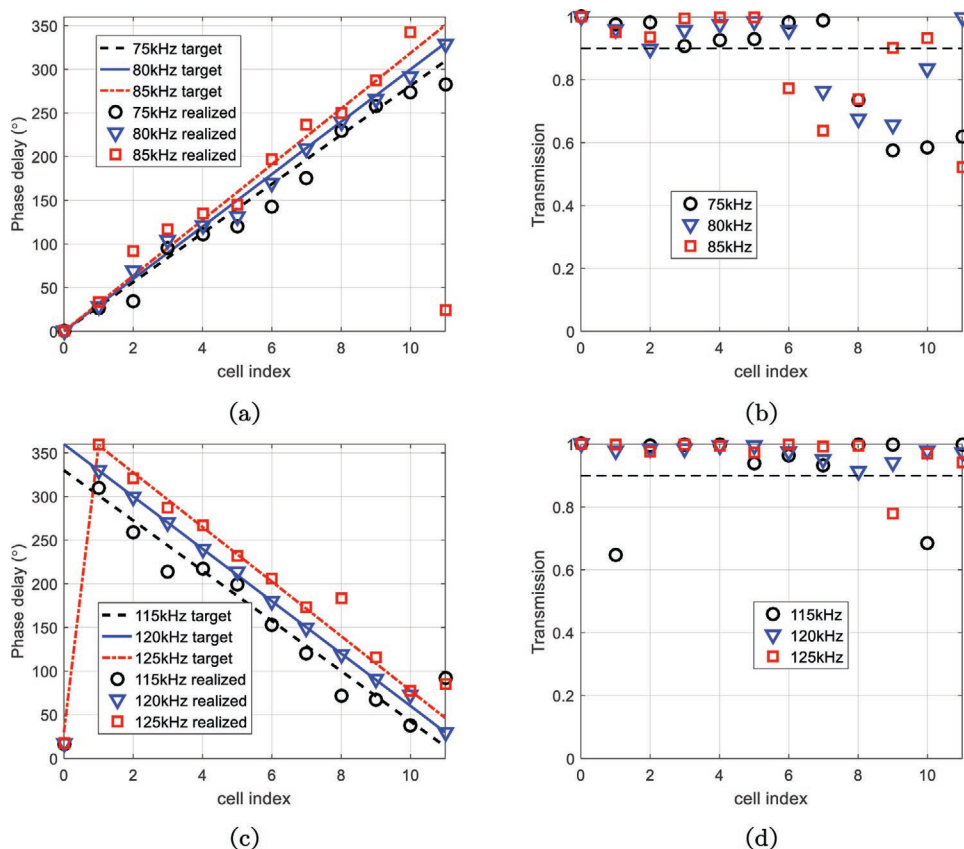
Figure 2. Realized and target phase shifts and transmission coefficients produced by unit cells listed in Table 1 at two frequency groups. a,b) At the frequency group centered at 80 kHz. c,d) at the frequency group centered at 120 kHz. The dashed lines in the transmission diagrams indicate the value of 0.9.

unit cell #6, the two frequencies lie in two different branches, formed by the hybridization of a local monopolar mode and a longitudinal mode (Figure 3b). These results show that the developed optimization algorithm is capable of engineering the wave dispersion so as to achieve target phase delays. The resulting structures of the optimized unit cells are very different
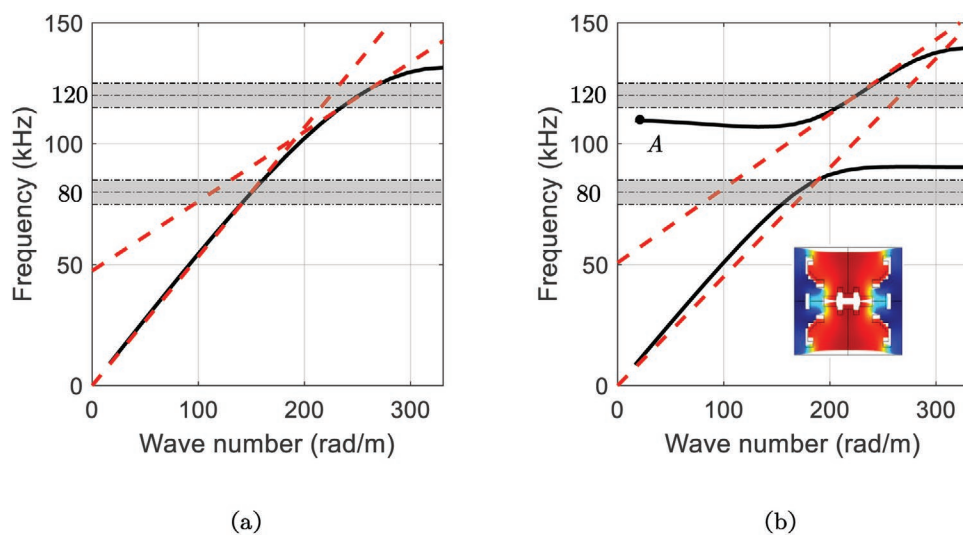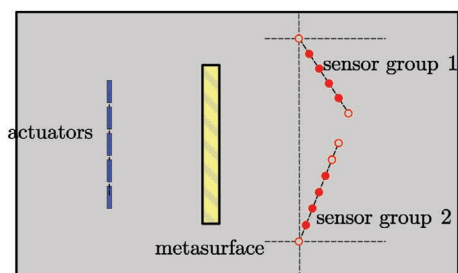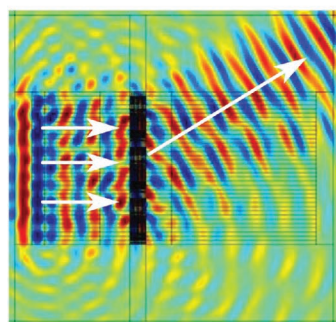

Figure 3. Dispersion band structures of unit cell a) #4 and b) #6 in Table 1. The red dashed lines denote target dispersion curves (Equation (5)) and the black solid lines denote achieved curves. The shaded areas illustrate the two frequency intervals centered at 80 and 120 kHz. The inset in (b) presents the mode shape (i.e., amplitude of the displacement field) and the deformed unit cell at the monopolar resonance, which corresponds to point A in the band curve.

ADVANCED
SCIENCE NEWS
www.advancedsciencenews.com

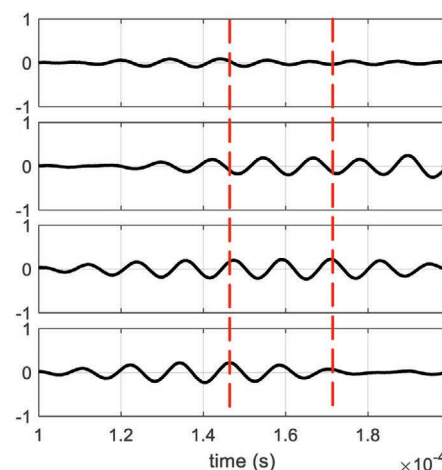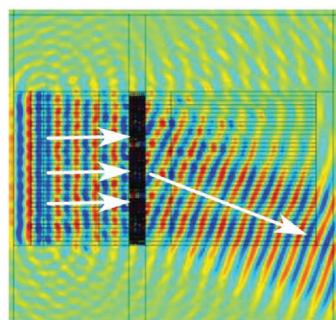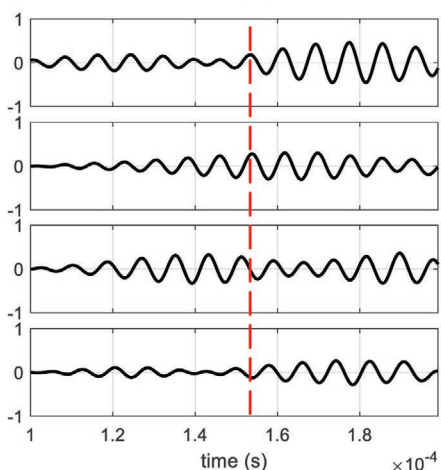ADVANCED
FUNCTIONAL
MATERIALS
www.afm-journal.de
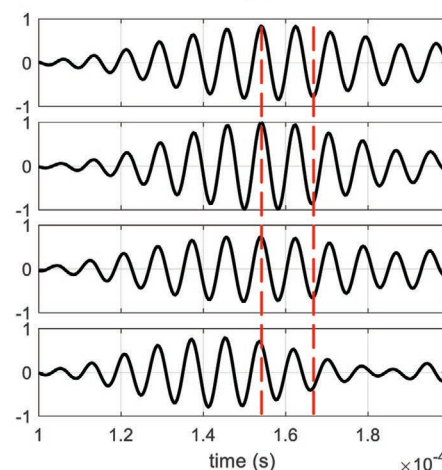
(a)
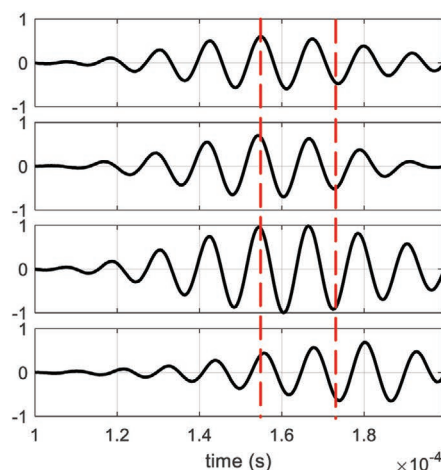
Figure 4. Simulation and experimental results for frequency-dependent wave beam steering. a) Configuration of sensors and actuators. b) Simulation results at 80 kHz. c) Signals received by sensors in Group 1 at 80 kHz. d) Signals received by sensors in Group 2 at 80 kHz. e) Simulation results at 120 kHz. f) Signals received by sensors in Group 1 at 120 kHz. g) Signals received by sensors in Group 2 at 120 kHz. For brevity, only signals of four sensors denoted by solid dots in (a) are presented in each group. Signals are normalized by the maximum value at each frequency.

from each other and achieve the target dispersion curves under different mechanisms. Such mixed-type designs would be difficult to obtain using common physics-guided approaches.

To demonstrate the function of the designed metasurface, full-wave simulations of waves propagating in the sandwiched configuration shown in Figure 1a were conducted. The metasurface consists of three supercells periodically arranged along the y direction. Longitudinal plane waves were excited from a line source with a harmonic force acting along the x direction. **Figure 4**b,e shows the simulated x component of displacement

**ADVANCED
SCIENCE NEWS**
www.advancedsciencenews.com

**ADVANCED
FUNCTIONAL
MATERIALS**
www.afm-journal.de

fields at 80 and 120 kHz, respectively. Clearly, the waves are guided into different directions at the two frequencies. The simulated angles of refraction are 32.1° and − 21.2°, respectively, which match quite well with the theoretical values. In addition, the wave manipulation is robust over frequency, as the angles of refractions remain nearly unchanged over the two frequency ranges designed (Section S1, Supporting Information). It should be mentioned that the designed refraction angles are not too large, so no noticeable mode conversion is observed.[45]

Experiments were conducted to validate the performance of the designed metasurface. A thin aluminum plate with dimensions of 1000 mm × 600 mm × 1 mm was used to comply with the plane stress assumption. In this case, the lowest symmetric lamb wave (S_0) is a good approximation for longitudinal wave used in the design. Metasurface was fabricated on the plate by laser precision cutting. Figure 4a schematically shows the configurations of the metasurface, sensors and actuators on the plate. An array of rectangular piezoelectric transducers (PZTs) with dimensions of 50 mm × 10 mm bonded on the left side of the plate were used to generate S_0 waves. On the right side of the plate, two groups of circular PZTs with diameters of 10 mm were used as sensors. Sensors in Group 1 were aligned with the expected wavefront of the transmitted wave at 80 kHz, while the other group of sensors were aligned with that at 120 kHz. The interval between each sensor is 4 cm. Note that although A_0 mode was also generated, but its wave velocity is considerably smaller than that of S_0 wave for the frequencies considered. Thus, by controlling the recording time interval, only S_0 mode was recorded.

The excitation signal used is a modulated 8 or 12 cycle burst centered at 80 or 120 kHz, generated by a function generator. Wave signals received by four sensors in each group are presented in Figure 4. Figure 4c,d shows signals received for the incident wave of 80 kHz, while Figure 4f,g show signals received for the incident wave of 120 kHz. As indicated by two red dash lines in Figure 4c, the peaks and valleys of all four received signals approximately align with each other in time, indicating that the received signals of sensors in Group 1 are approximately in phase at 80 kHz. The same phenomenon also occurs for sensors in Group 2 at 120 kHz, as can be observed in Figure 4g. On the contrary, signals presented in Figure 4d,f, which record the waves at locations that are not aligned with the expected wavefronts, are not in phase. These observed phenomena verify that wavefronts of refracted waves at two frequencies are indeed aligned with the designed wavefronts. In addition, for 80 kHz waves, signal amplitudes of sensors in Group 2 were considerably smaller than those received by sensors of Group 1, indicating that most of the refracted wave was steered into the designed direction. The same can be observed for the refracted wave of 120 kHz in which signal amplitudes of sensors in Group 1 were considerably smaller than those received in sensors of Group 2.

2.2.2. Frequency-Dependent Wave Focusing

The proposed optimization method can be used to design metasurfaces with many different functionalities. Wave focusing is needed in a number of application areas including

energy harvesting,[46] ultrasound therapies[47] and microfluidic control.[48] In the second example, we demonstrate a metasurface that can focus waves onto different points via changing operation frequencies.

To achieve this, two different hyperbolic phase profiles were realized on one metasurface at 80 and 120 kHz, respectively. Each of them the form of

$$\phi_i(y) = \frac{\omega_{ci}}{v_0} \sqrt{(x_{ci})^2 + (y - y_{ci})^2} \tag{6}$$

where the y axis is defined to align with the right interface between the metasurface and the host material. v_0 is the wave velocity in the host material. (x_{ci}, y_{ci}) denote the coordinates of the desired focal point at operating frequency ω_{ci}. In this example, two well-separated points, $P_1 = (25 - 9\ \text{cm})$ and $P_2 = (25,\ 9\ \text{cm})$, are selected as focal points at 80 and 120 kHz, respectively. Forty-five unit cells realizing different phase delays at the target frequencies were designed and their structures are shown in Section S2 in the Supporting Information. **Figure 5** plots the target and realized phase shift profiles and transmissions at different target frequencies. Similar to the previous example, the realized phase shifts match well with target values and the average transmission coefficients are 0.9 at 80 kHz and 0.95 at 120 kHz, respectively.

Simulations and experiments were conducted at two center frequencies to verify the function of the designed metasurface. As shown in **Figure 6**a, sensors were mounted along two lines, which are perpendicular to OP_1 and OP_2, with O being the center point of the right interface. Totally five sensors were used along each line, with an interval of 3 cm between two neighboring sensors. Results are presented in Figure 6d–g. In both cases, wave focusing on the desired locations, i.e., P_1 and P_2, can be clearly observed from the simulated displacement fields shown in Figure 6b,c. It should be noted that when the refraction angle is large, there will be a notable mode conversion from longitudinal waves to shear horizontal waves. As labeled by red circles in Figure 6b,c, the converted shear waves are not focused on the desired locations because their refraction angles are different from those of the longitudinal waves. This is inevitable in elastic metasurfaces due to mode conversion.[45] Despite that, a large portion of the wave energy is focused at the desired point P_1 or P_2 in the two cases, which can be seen from the significantly large amplitude observed in the focused region as compared to that in other region. To provide quantitative comparison, wave amplitudes along the two lines are plotted in Figure 6d–g. Overall experimental results agree well with simulation results in terms of the focusing phenomena except at a few points. The discrepancies at these points are likely caused by the nonideal measurement conditions. For example, the interactions between PZT sensors. Both simulations and experiments show around five times difference in wave amplitude between P_1 and P_2 at each target frequency.

3. Discussions

Based on the topology optimization method, we have designed and experimentally demonstrated novel metasurfaces, which

ADVANCED
SCIENCE NEWS
www.advancedsciencenews.com

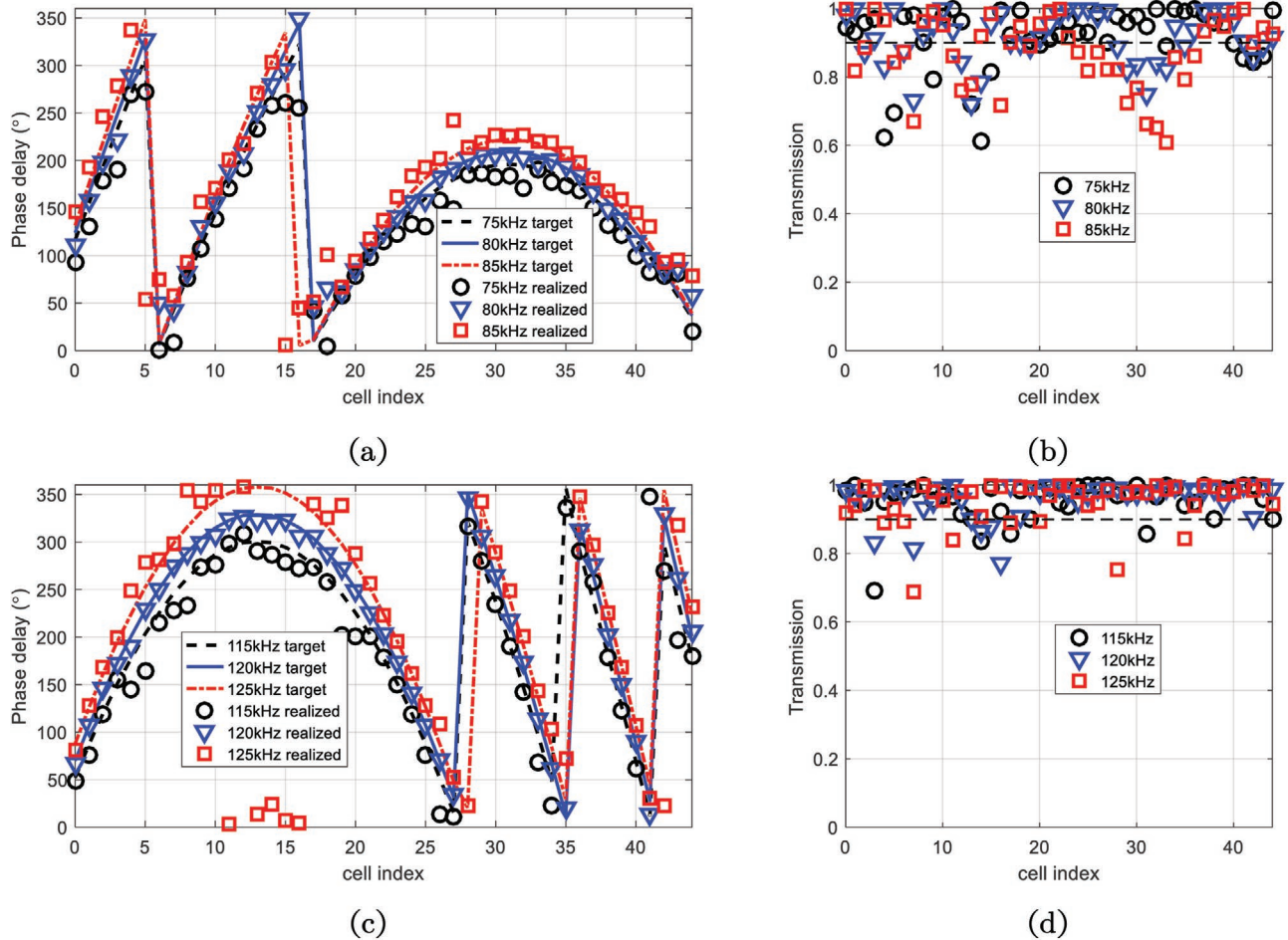ADVANCED
FUNCTIONAL
MATERIALS
www.afm-journal.de

Figure 5. Realized and target phase profiles and transmission coefficients of the metasurface designed for wave focusing at two frequency groups. a,b) For waves centered at 80 kHz. c,d) For waves centered at 120 kHz. The dashed lines in the transmission diagrams indicate the value of 0.9.

possess of multiple functions at different operation frequencies. These materials are purely passive and the function switch is achieved by simply changing the operation frequency, therefore enabling on-demand control of elastic wave propagation. Compared to some reconfigurable and programmable metamaterials developed recently, our designs are free of geometrical change when switching the functions and do not need a complex control system. As an illustration, a metasurface that can selectively steer a normally incident wave into two different directions or focus the wave onto two well-separated points was demonstrated. The proposed design methodology is however able to encode more functionalities onto one single metasurface. A metasurface that selectively steer a normally incident wave into three different directions at three frequencies was also designed, fabricated and experimentally validated. Results are listed in Section S3 in the Supporting Information. In addition, different combinations of functionalities, for example, sterring and focusing, can be encoded onto the same metasurface.

Although the proof-of-concept examples presented in this paper are designed for bulk waves under the plane stress condition, the design methodology can be easily extended to handle other types of waves, such as surface acoustic waves. With

further development, we expect the proposed frequency-coded metasurface concept can be applied in a variety of applications that require flexible elastic wave manipulation, including acoustic hologram, microfluidic manipulation and acoustic tweezers. In particular, the development of acoustic tweezers, which have attracted great interests for their capabilities of moving, trapping, separating and patterning microparticles,[10] can benefit from the proposed method. Compared to phased array systems that are complex, bulky and expensive for on-chip applications,[49] metasurface-based acoustic tweezers have the advantages in their compact form, low cost and can be easily scaled down. However, most of existing designs are lack of tunability. The frequency-coded design approach would enable them a certain degree of tunability, thus allowing for dexterous and selective wave manipulation and helping to develop more compact and multifunctional devices.

One drawback of the current method is that some designed unit cells have rather complex structures, which may cause difficulties in fabrication. This could be addressed with manufacturing oriented topology optimization methods.[50,51] For example, the feature-driven topology optimization, in which optimal structures are composed of components that are manufacture-friendly.[52,53] We also mention the recently proposed
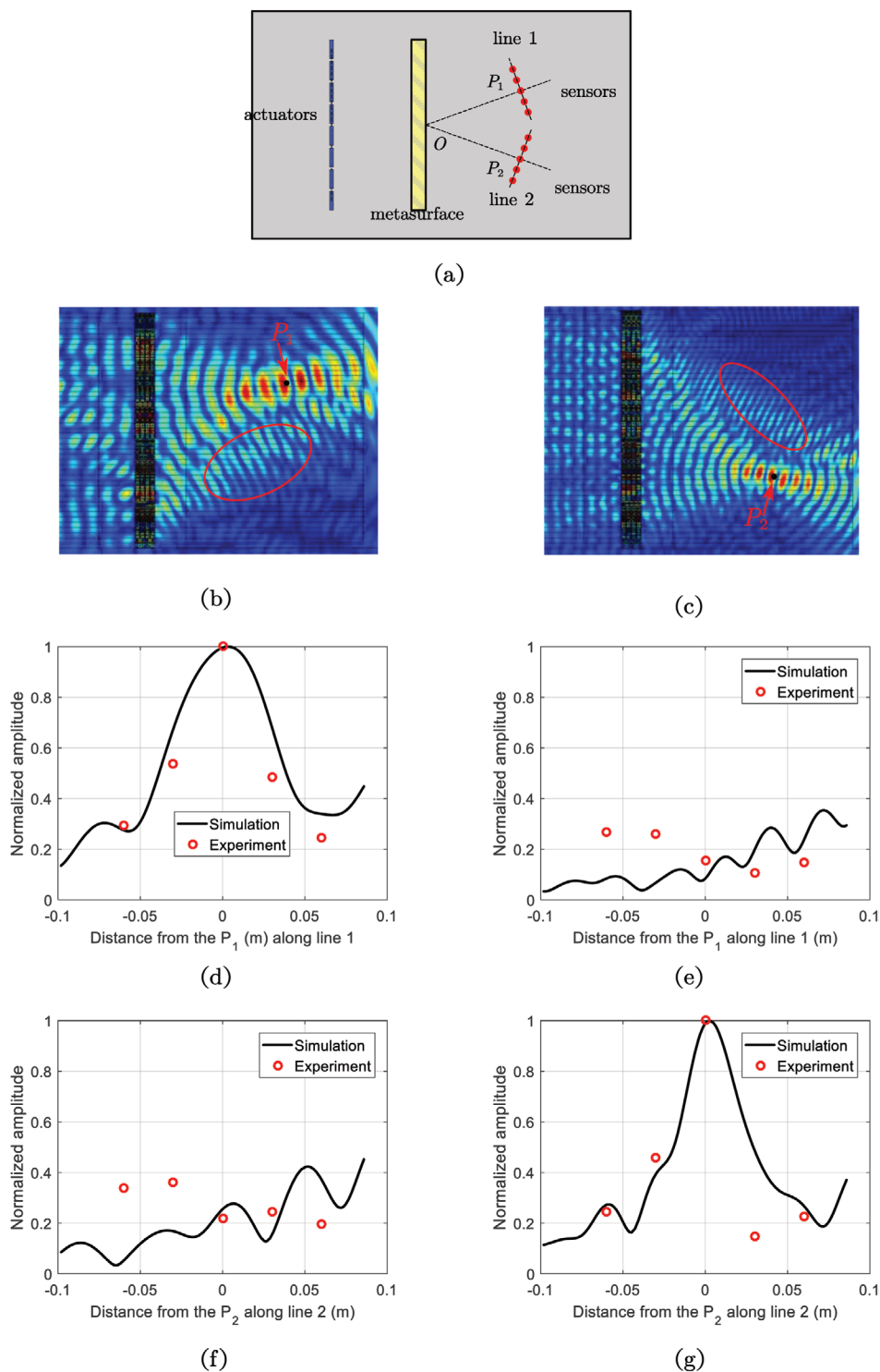
Figure 6. a) Schematics of the measurement setup. b) Simulated total displacement field ($\sqrt{u_r^2 + v_r^2}$, where u_r and v_r are real parts of the x and y components of the displacement field) at b) 80 kHz and c) 120 kHz; Amplitude of displacement along line 1 at d) 80 kHz and e) 120 kHz. Negative distance values means the location is above P_1. Amplitude of displacement along line 2 at f) 80 kHz and g) 120 kHz. Negative distance means the location is below P_2. All amplitudes are normalized by their maximum values at the corresponding frequency.

machine learning based inverse design methods,[54–56] which use deep generative models to ensure the obtained structures are manufacturable.

4. Experimental Section

Measurement Setup: The metasurface samples were fabricated on an aluminum plate via high precision laser fiber cutting machine (Glorystar
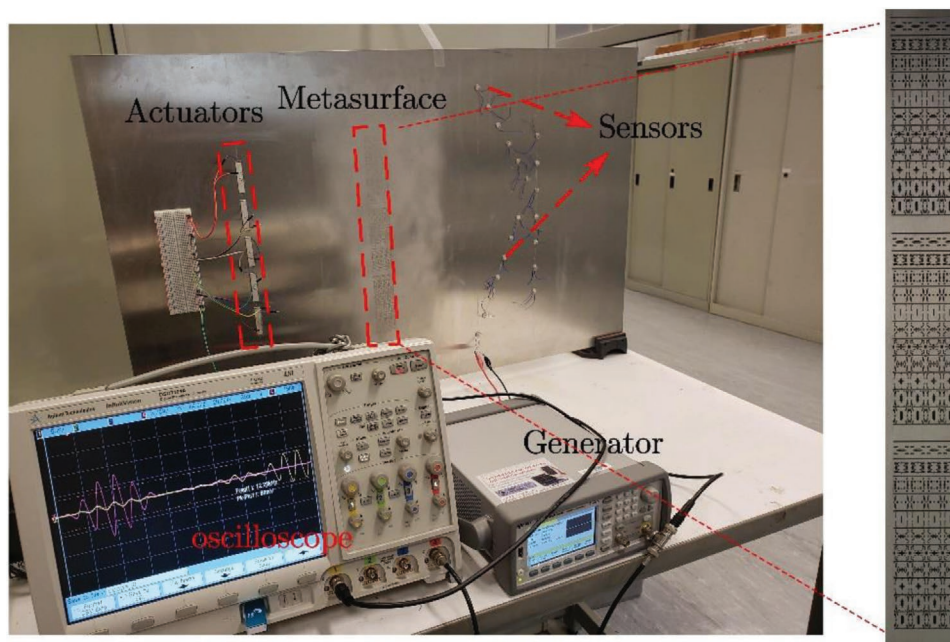
Figure 7. Experimental setup. The inset on the right side shows an enlarged figure of the fabricated metasurface in Section 2.2.1.

GS-0605P). The experimental setting is shown in **Figure 7**. The elastic waves were excited by PZTs with signals inputted from a functional generator (Keysight 33500B) and detected by PZT sensors. A digital oscilloscope (Agilent DSO7104A) was used to record wave signals. The placements of actuators, sensors, and metasurface were carefully designed in order to prevent any reflected wave from boundaries to disturb the received signals within the recorded time interval and to ensure that the incident wave was approximately plane wave.

Topology Optimization: In this work, the transmission coefficient T and phase delay ϕ of wave transmitting through one row of metamaterial was computed by the finite element method via a one-row sandwiched model as shown in Figure 1a. Genetic algorithm (GA) based topology optimization was adopted to find the solution of the inverse problem. Each binary chromosome involved in the GA corresponded to a unit cell structure formed by a uniform finite element mesh. And each gene in a chromosome corresponded to one finite element regarding the material phase 1 (solid) and 0 (void). The search space of this optimization had $2^{N_c \times N_e}$ possible structures, where N_e denotes the number of finite elements. To reduce the design space, the structure of the unit cell was assumed to be orthogonally symmetric, and thus only one quarter was needed for optimization. To further reduce the design space and eliminate unviable designs such as those contain disconnected components or thin connections, some topology repairing techniques were employed, including abuttal entropy filtering, penalties over structural connectivity and thin components. In all the design cases, the optimization started from a random initial structure. According to the experience, changing initial structures resulted in different optimized results, but their performances were generally similar. For a detailed description on the method, the readers are referred to ref. [45]. In Section S4 in the Supporting Information, an example is given to show the evolution history of the objectives and unit cells structures during the optimization procedure.

Supporting Information

Supporting Information is available from the Wiley Online Library or from the author.

Conflict of Interest

The authors declare no conflict of interest.

[1] N. Yu, P. Genevet, M. A. Kats, F. Aieta, J. P. Tetienne, F. Capasso, Z. Gaburro, *Science* **2011**, *334*, 333.

[2] Y. Xie, W. Wang, H. Chen, A. Konneker, B. I. Popa, S. A. Cummer, *Nat. Commun.* **2014**, *5*, 5553.

[3] Y. Liu, Z. Liang, F. Liu, O. Diba, A. Lamb, J. Li, *Phys. Rev. Lett.* **2017**, *119*, 034301.

[4] J. Zhang, X. Zhang, F. Xu, X. Ding, M. Deng, N. Hu, C. Zhang, *J. Sound Vib.* **2020**, *481*, 115440.

[5] H. Zhu, T. F. Walsh, F. Semperlotti, *Appl. Phys. Lett.* **2018**, *113*, 221903.

[6] L. Cao, Z. Yang, Y. Xu, S.-W. Fan, Y. Zhu, Z. Chen, Y. Li, B. Assouar, *J. Mech. Phys. Solids* **2020**, *143*, 104052.

[7] J. Zhang, Y. Tian, Y. Cheng, X. Liu, *Appl. Phys. Lett.* **2020**, *116*, 030501.

**ADVANCED
SCIENCE NEWS**

www.advancedsciencenews.com

**ADVANCED
FUNCTIONAL
MATERIALS**

www.afm-journal.de

[8] S.-W. Fan, S.-D. Zhao, L. Cao, Y. Zhu, A. L. Chen, Y.-F. Wang, K. Donda, Y.-S. Wang, B. Assouar, *Phys. Rev. B* **2020**, *101*, 024104.

[9] S. Tol, F. L. Degertekin, A. Erturk, *Addit. Manuf.* **2019**, *29*, 100780.

[10] A. Ozcelik, J. Rufo, F. Guo, Y. Gu, P. Li, J. Lata, T. J. Huang, *Nat. Methods* **2018**, *15*, 1021.

[11] P. Wang, F. Casadei, S. Shan, J. C. Weaver, K. Bertoldi, *Phys. Rev. Lett.* **2014**, *113*, 014301.

[12] S. Babaee, N. Viard, P. Wang, N. X. Fang, K. Bertoldi, *Adv. Mater.* **2016**, *28*, 1631.

[13] O. R. Bilal, A. Foehr, C. Daraio, *Adv. Mater.* **2017**, *29*, 1700628.

[14] Z. Hou, B. M. Assouar, *Appl. Phys. Lett.* **2015**, *106*, 251901.

[15] S. Shan, S. H. Kang, P. Wang, C. Qu, S. Shian, E. R. Chen, K. Bertoldi, *Adv. Funct. Mater.* **2014**, *24*, 4935.

[16] M. Schaeffer, M. Ruzzene, *J. Appl. Phys.* **2015**, *117*, 193101.

[17] Z. Zhao, C. Yuan, M. Lei, L. Yang, Q. Zhang, H. Chen, H. J. Qi, D. Fang, *Phys. Rev. Appl.* **2019**, *11*, 044074.

[18] S. Babaee, J. T. Overvelde, E. R. Chen, V. Tournat, K. Bertoldi, *Sci. Adv.* **2016**, *2*, 1601019.

[19] G. Memoli, M. Caleap, M. Asakawa, D. R. Sahoo, B. W. Drinkwater, S. Subramanian, *Nat. Commun.* **2017**, *8*, 14608.

[20] Z. Tian, C. Shen, J. Li, E. Reit, Y. Gu, H. Fu, S. A. Cummer, T. J. Huang, *Adv. Funct. Mater.* **2019**, *29*, 1808489.

[21] S.-D. Zhao, A. L. Chen, Y.-S. Wang, C. Zhang, *Phys. Rev. Appl.* **2018**, *10*, 054066.

[22] S.-W. Fan, S.-D. Zhao, A. L. Chen, Y.-F. Wang, B. Assouar, Y.-S. Wang, *Phys. Rev. Appl.* **2019**, *11*, 044038.

[23] S.-M. Yuan, A. L. Chen, Y.-S. Wang, *J. Sound Vib.* **2020**, *470*, 115168.

[24] S. Li, J. Xu, J. Tang, *Appl. Phys. Lett.* **2018**, *112*, 021903.

[25] Y. Chen, X. Li, H. Nassar, G. Hu, G. Huang, *Smart Mater. Struct.* **2018**, *27*, 115011.

[26] J. Cha, K. W. Kim, C. Daraio, *Nature* **2018**, *564*, 229.

[27] S. Chen, W. Liu, Z. Li, H. Cheng, J. Tian, *Adv. Mater.* **2020**, *32*, 1805912.

[28] B. Xiong, L. Deng, R. Peng, Y. Liu, *Nanoscale Adv.* **2019**, *1*, 3786.

[29] A. Darabi, M. J. Leamy, *Phys. Rev. Appl.* **2019**, *12*, 044030.

[30] F. Yue, D. Wen, C. Zhang, B. D. Gerardot, W. Wang, S. Zhang, X. Chen, *Adv. Mater.* **2017**, *29*, 1603838.

[31] S. Liu, T. J. Cui, Q. Xu, D. Bao, L. Du, X. Wan, W. X. Tang, C. Ouyang, X. Y. Zhou, H. Yuan, H. F. Ma, W. X. Jiang, J. Han, W. Zhang, Q. Cheng, *Light: Sci. Appl.* **2016**, *5*, 16076.

[32] O. Avayu, E. Almeida, Y. Prior, T. Ellenbogen, *Nat. Commun.* **2017**, *8*, 14992.

[33] B. Wang, F. Dong, Q. T. Li, D. Yang, C. Sun, J. Chen, Z. Song, L. Xu, W. Chu, Y. F. Xiao, Q. Gong, Y. Li, *Nano Lett.* **2016**, *16*, 5235.

[34] M. Qiu, M. Jia, S. Ma, S. Sun, Q. He, L. Zhou, *Phys. Rev. Appl.* **2018**, *9*, 054050.

[35] D. Wen, F. Yue, G. Li, G. Zheng, K. Chan, S. Chen, M. Chen, K. F. Li, P. W. Wong, K. W. Cheah, E. Y. Pun, S. Zhang, X. Chen, *Nat. Commun.* **2015**, *6*, 8241.

[36] X. Chen, P. Liu, Z. Hou, Y. Pei, *Appl. Phys. Lett.* **2017**, *110*, 053101.

[37] Y. Zhu, B. Assouar, *Phys. Rev. B* **2019**, *99*, 053101.

[38] Y. Zhu, B. Assouar, *Phys. Rev. Mater.* **2019**, *3*, 045201.

[39] H. Lee, J. K. Lee, H. M. Seung, Y. Y. Kim, *J. Mech. Phys. Solids* **2018**, *112*, 577.

[40] N. Aage, E. Andreassen, B. S. Lazarov, O. Sigmund, *Nature* **2017**, *550*, 84.

[41] H.-W. Dong, S.-D. Zhao, P. Wei, L. Cheng, Y.-S. Wang, C. Zhang, *Acta Mater.* **2019**, *172*, 102.

[42] Y. Chen, F. Meng, G. Li, X. Huang, *Acta Mater.* **2019**, *164*, 377.

[43] G. Oliveri, J. T. B. Overvelde, *Adv. Funct. Mater.* **2020**, *30*, 1909033.

[44] R. E. Christiansen, F. Wang, O. Sigmund, *Phys. Rev. Lett.* **2019**, *122*, 234502.

[45] J. Rong, W. Ye, *Acta Mater.* **2020**, *185*, 382.

[46] S. Tol, F. L. Degertekin, A. Erturk, *Appl. Phys. Lett.* **2016**, *109*, 063902.

[47] S. Jiménez-Gambín, N. Jiménez, J. M. Benlloch, F. Camarena, *Phys. Rev. Appl.* **2019**, *12*, 014016.

[48] D. J. Collins, Z. Ma, J. Han, Y. Ai, *Lab Chip* **2017**, *17*, 91.

[49] A. Riaud, M. Baudoin, O. Bou Matar, L. Becerra, J.-L. Thomas, *Phys. Rev. Appl.* **2017**, *7*, 024007.

[50] J. Liu, Y. Ma, *Adv. Eng. Software* **2016**, *100*, 161.

[51] W. Zhang, Y. Liu, P. Wei, Y. Zhu, X. Guo, *Comput. Methods Appl. Mech. Eng.* **2017**, *324*, 149.

[52] W. Zhang, J. Yuan, J. Zhang, X. Guo, *Struct. Multidisc. Optim.* **2016**, *53*, 1243.

[53] Y. Zhou, W. Zhang, J. Zhu, Z. Xu, *Comput. Methods Appl. Mech. Eng.* **2016**, *310*, 1.

[54] W. Ma, F. Cheng, Y. Xu, Q. Wen, Y. Liu, *Adv. Mater.* **2019**, *31*, 1901111.

[55] R. K. Tan, N. L. Zhang, W. Ye, *Struct. Multidisc. Optim.* **2020**, *61*, 1417.

[56] Y. Zhang, W. Ye, *Struct. Multidisc. Optim.* **2019**, *60*, 527.